Surface versus internal fatigue crack initiation in steel: Influence of mean stress

Vidit Gaur [a,b], Véronique Doquet [a,*], Emmanuel Persent [b], Charles Mareau [c], Eléonore Roguet [b], Jean Kittel [d]

[a] LMS, Ecole Polytechnique, Université Paris-Saclay, UMR CNRS 7649, Palaiseau, France
[b] IFP Energies Nouvelles, 1 et 4 avenue de Bois-Préau, 92852 Rueil-Malmaison, France
[c] LAMPA, Arts et Métier Paris Tech, 2 Boulevard du Ronceray, 49035 Angers, France
[d] IFP Energies Nouvelles, rond-point de léchangeur de Solaize, BP3 69360 Solaize, France

A B S T R A C T

Stress-controlled fatigue tests were run at different R ratios ($= \sigma_{min}/\sigma_{max}$) up to at most 3 million cycles on a 2.5%Cr–1%Mo steel (ASTM A182 F22) used in riser tubes connectors for offshore oil drilling. The fatigue lives, as well as the slope of the S–N curves were found to decrease with increasing R and the endurance limit to follow Gerber's parabola. Surface crack initiation without any defect involved, was most often observed for $R = -1$, -0.5 and 0, while an R ratio of 0.25 triggered crack initiation from either surface or internal pores or chemically inhomogeneous areas, leading, in the latter case, to fish-eye patterns for relatively low numbers of cycles. A further increase in R ratio to 0.5 promoted only defect-initiated surface cracks, while no fatigue fracture was observed within 10 million cycles above $R = 0.6$. These transitions in crack initiation mode are discussed based on X-ray diffraction analyses of residual stresses, elastic–plastic F.E. computations on a unit cell model containing a pore and some fracture mechanics analyses, with a particular attention to environmental effects.

Keywords:
Mean stress
Internal crack
Steel
Defects
Fish-eye

1. Introduction

Fatigue cracks are known to initiate potentially in steels by a variety of mechanisms: from the surface at machining marks, persistent slip bands, grain/phase boundaries or surface-cutting defects, or from internal metallurgical defects. Surface initiation usually predominates up to 10^6 cycles, while internal crack initiation is common in the very high cycle fatigue (VHCF) (>10^7 cycles) [1–5]. The switch from surface to internal crack initiation often leads to dual S–N curve [6,7] with a plateau between 10^6 and 10^7 cycles, which has long been considered as the endurance limit, (since surface-initiated cracks do not propagate below this stress amplitude) until the use of ultrasonic testing machines revealed fatigue failures from internal defects, at even lower stress ranges, i.e. VHCF.

Internal crack initiation is generally accompanied by a "fish-eye" pattern on the fracture surface [8–10] and often, by a rough Optically Dark Area (ODA) [9], also called Fine Granular Area (FGA) [7], surrounding the defect responsible for crack initiation. The formation mechanism of the ODA/FGA has been much debated [9–12]. The formation of an ODA/FGA is known to require at least 10^7 fatigue cycles, under fully reversed loading. Surface residual stresses have been reported to play an important role in the competition between surface and internal crack initiation [13–15]. Compressive surface residual stresses were reported to inhibit surface crack initiation when they are stable and thus to favor internal crack initiation.

Many attempts to use Linear Elastic Fracture Mechanics (LEFM) to predict the endurance limit in case of internal crack initiation, based on the defects size distribution and a threshold ΔK for fatigue crack growth, or to compute the fraction of fatigue life spent in internal crack growth by integration of crack growth kinetics, can be found in the literature [1,5]. The main difficulty with these approaches is the lack of reliable data on fatigue crack growth threshold and kinetics for the environmental conditions encountered by internal cracks. The latter is, however, controversial as some authors consider that internal cracks grow in vacuum [10], while some others [9] consider that gases trapped at the internal defect from which the crack initiates (moist air or hydrogen), can diffuse into the metal during VHCF and assist its growth.

Murakami [16] proposed an empirical equation to estimate the endurance limit as a function of the R ratio for the failures initiated from internal inclusions ($C = 1.56$ in Eq. (1a)) or inclusions touching the surface ($C = 1.41$ in Eq. (1a)) based on the Vickers hardness,

* Corresponding author.
E-mail addresses: gaur.vidit@gmail.com (V. Gaur), doquet@lms.polytechnique.fr (V. Doquet).

H_V and the area of the largest inclusion (estimated from the statistics of extremes) projected on the first principal plane:

$$\sigma_w = \frac{C(H_V + 120)}{(\sqrt{area})^{1/6}} \left[\frac{1-R}{2}\right]^{\alpha} \quad (1a)$$

$$\alpha = 0.226 + H_V \times 10^{-4} \quad (1b)$$

Unfortunately, most of the tests giving rise to fish-eye patterns reported so far have been performed at $R = -1$ because ultrasonic testing machines are basically designed for such loading and have to be modified to allow positive mean stresses ($R > 0$). Very few studies [16,17] are available regarding the influence of a mean stress on internal fatigue crack initiation and growth from natural defects.

The present study will thus contribute to fill this gap. This work is a part of an ongoing study on corrosion-fatigue in offshore oil drilling structures, more specifically "clip connectors" designed at Institut Français du Pétrole et des Energies Nouvelles (IFPEN) to connect/disconnect conveniently the riser tubes [18]. The assembly experiences external pressure from sea water, internal pressure of the fluid flowing through it, the mass of the riser, buoyancy force and above all, sea waves which induce cyclic bending and potentially, fatigue damage. It is subjected to two different conditions: the "connected mode" with a high mean stress ($R = 0.7$) and low amplitude constituting more than 90% of the service life and the "disconnected mode" with a lower mean stress ($R = 0.2$) but higher amplitude constituting less than 10% of the service life.

In order to determine a suitable fatigue criterion to assess the durability of these structures, push–pull tests were run under various R ratios. The characterization was not limited to the range $R = 0.2$–0.7, but also included some fully-reversed loadings ($R = -1$) because the corresponding endurance limit was needed to calibrate various fatigue criteria. Tests were also run at $R = -0.5$ and 0, because the service load on a connector is variable in terms of amplitude and R ratio, and 0.2 is only an average value for the "disconnected mode". In spite of the relatively low number of cycles ($<3 \times 10^6$), an increase in R ratio from 0 to 0.25 promoted defect-initiated cracks, either internal or from the surface, while a further increase to $R = 0.5$ led only to defect-initiated surface cracks. These transitions are discussed based on X-ray diffraction (XRD) analyses of residual stresses, elastic–plastic finite element (FE) computations on a unit cell model containing a pore and some tentative fracture mechanics analyses.

2. Experimental study

2.1. Material

The ASTM A182 F22 2.5%Cr–1%Mo steel which constitutes the clip connectors has the measured chemical composition as shown in Table 1 and the tensile properties shown in Table 2. After austenitization between 940 °C and 970 °C, the material was water-quenched and finally tempered at 625 °C. The microstructure revealed by etching (10 s) in a 5% nitric acid in ethanol after mechanical polishing down to 3 μm roughness is shown in Fig. 1. This microstructure is representative of the fatigue specimens mentioned below, since it was observed, without any significant variation on all the faces of several cubical samples cut at various places in a 21″ lock ring male clip connector provided by Aker Solutions, which had not been used in service before. The microstructure is a non-textured, aged martensite, with 6.5–7.7 μm wide equiaxed grains containing remnants of laths. Aluminum–magnesium–calcium oxide and manganese sulfide inclusions with an average size of 5 μm are present, but do not seem harmful in fatigue, contrary to some less frequent but larger (40–300 μm) pores and inhomogeneous zones, as illustrated and discussed later.

Table 1
Measured chemical composition of F22 alloy steel (weight %).

C	Cr	Mo	O	Mn	Si	Ni	Cu
3.5	2.5	1.1	1.4	0.6	0.2	0.1	0.1

Table 2
Basic mechanical properties of F22 alloy steel.

Proportional limit (MPa)	0.2% Yield stress (MPa)	Ultimate tensile stress (MPa)	Vickers hardness (HV 300)
600	694	780	267

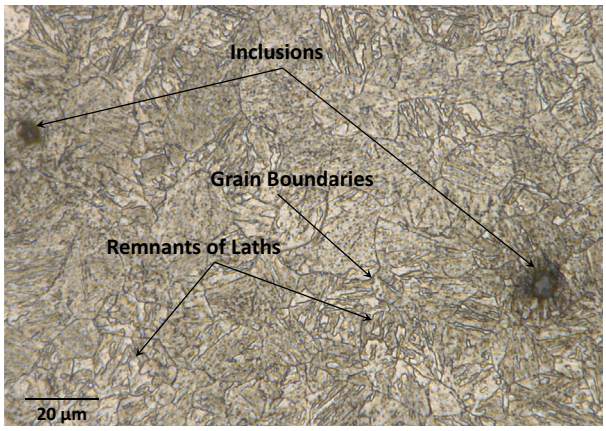

Fig. 1. Microstructure of F22 alloy steel.

2.2. Experimental procedures

Cylindrical specimens were cut along the longitudinal direction, at the same axial and radial positions, all round the male part of the clip connector mentioned above. No difference in potential segregation of alloying elements or impurities is thus expected among these specimens. The specimen diameter (Fig. 2) was $D = 8$ mm for the fatigue tests run at $R = -1$, -0.5 and 0. But the reduction in section between the gage length and threaded head was insufficient to avoid crack initiation in the threads at higher mean stresses. Specimens with a gage diameter, $D = 7$ mm were thus used for fatigue tests at $R = 0.25$ and $D = 6$ mm for $R = 0.5$, 0.6 and 0.7. The gage plus shoulder fillet length was kept same for all the specimens. The surface roughness R_a was less than 0.4 μm. With such geometries, fatigue failure (defined as complete sample separation) always occurred within the gage length. A 100 kN MTS 810 testing machine with a FlexTest 40 controller and BasicTestware software was used for load-controlled push–pull tests at different R ratios (-1, -0.5, 0, 0.25, 0.5, 0.6 and 0.7) in air at 10 Hz. Careful preliminary alignment of the upper and lower grips was done using a stiff, calibrated piece. Most of the tests were stopped at 3×10^6 cycles and the corresponding stress amplitude was considered as the endurance limit for that R ratio. However, the tests at $R = 0.6$ and 0.7 were continued until 10^7 cycles.

Fracture surface observations as well as Energy Dispersive Spectrometry (EDS) chemical micro-analysis around the crack initiation sites were done using a FEI Quanta 600 Field Emission Gun-SEM. A Keyence digital optical microscope was used for topographic measurements around the crack initiation sites. A few detailed observations were done after platinum deposit and Field

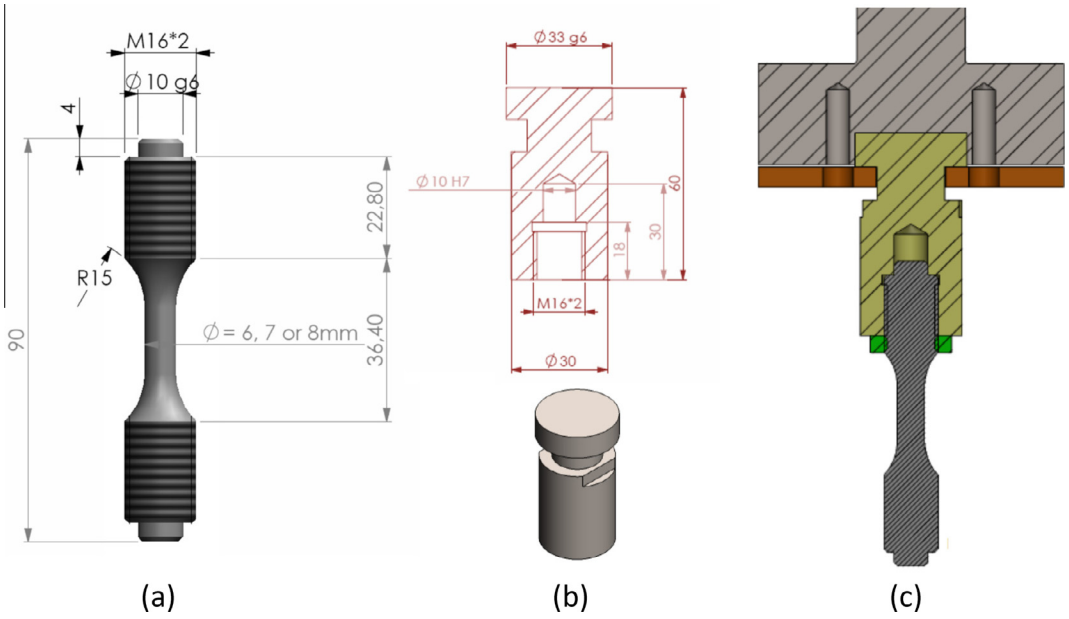

Fig. 2. (a) Specimen geometry, (b) griping device and (c) complete assembly.

Ion Beam (FIB) sectioning, using a FEI Helios 660 dual-beam microscope at Ecole Centrale Paris.

The residual stresses left by machining in the near surface layers of the specimens were estimated using XRD techniques. The XRD analyses were performed with a PROTO iXRD diffractometer [19] equipped with a Cr anode. For this anode material, the penetration depth (63% of absorption) of X-rays in steel is about 5 µm. The peak positions associated with {2 1 1} planes were measured with two scintillation detectors with a 2θ range of 18.5° each. For each analyses, the irradiated zone was delimited with a circular collimator (0.5 mm diameter). Residual stresses were estimated from peak positions using the $\mathrm{Sin}^2\psi$ method [20]. The X-ray elastic constants ($s_1 = -1.28 \times 10^{-6}$ MPa^{-1} and $\frac{1}{2}s_2 = 5.83 \times 10^{-6}$ MPa^{-1}) identified for α-ferrite were used for calculating the residual stress state. A preliminary calibration of the device and of the post-treatment parameters done on F22 steel powder (without residual stresses) had shown that the positions of the diffraction peaks are consistent with these elastic constants. For virgin specimens, the analyses were done for three equally-spaced surface points along the periphery, at mid-height of the gage length. To estimate the in-depth distribution of longitudinal residual stresses, successive material removal operations up to a depth of 150 µm were performed using an electrochemical polishing technique with a solution of salted water. To determine whether the residual stresses persist after the fatigue tests or not, some analyses were done on broken specimens, as far as possible (>6 mm) from the fracture surface, along the gage length.

2.3. Experimental results

2.3.1. Fatigue lives and crack initiation mechanisms

All tests parameters and results are reported in Table 3. Both the endurance limit and the slope of the *S–N* curves drop with increasing *R* ratio (Fig. 3). A Goodman plot (Fig. 4) shows that Gerber's parabola [21] provides the most accurate prediction of the endurance limit at different *R* ratios. At very high *R* ratios ($R = 0.6$ or 0.7), the specimens did not fail at all within 10^7 cycles.

All fatigue failures at $R = -1$, as well as 60% of the failures at $R = -0.5$ and 100% of the failures at $R = 0$ initiated from the surface, without any metallurgical or machining defect detected in the crack initiation area. SEM observations of longitudinal sections cut from specimens broken after a few thousands cycles under such *R* ratios, show secondary surface micro-cracks which initiated

Table 3
Test data obtained from high-cycle fatigue tests in air at 10 Hz, σ_a is the applied stress amplitude.

σ_a, MPa	*R* ratio	Cycles to failure, N_f	Initiation type
435	−1	193,620	Surface without defect
410	−1	367,166	Surface without defect
385	−1	1,137,624	Surface without defect
370	−1	521,343	Surface without defect
365	−1	>3,000,000	–
390	−0.5	322,888	Surface without defect
378	−0.5	390,914	Surface without defect
375	−0.5	182,856	Surface without defect
365	−0.5	741,938	Internal Pore with fish-eye
360	−0.5	2,207,630	Internal Pore with fish-eye
350	−0.5	>3,000,000	–
322	0	21,064	Surface without defect
318.5	0	153,518	Surface without defect
315	0	833,695	Surface without defect
310	0	198,067	Surface without defect
300	0	>3,000,000	–
273	0.25	228,359	Surface without defect
270	0.25	160,277	Internal Inhomogeneity
265	0.25	>3,000,000	–
260	0.25	1,704,174	Internal Pore
260	0.25	373,933	Internal Inhomogeneity
255	0.25	300,333	Internal Inhomogeneity
250	0.25	>3,000,000	–
250	0.25	339,602	Surface Pore
245	0.25	>3,000,000	–
240	0.25	>3,000,000	–
193	0.5	163,919	Machining mark
190	0.5	459,584	Machining mark
190	0.5	279,630	Machining mark
187	0.5	>3,000,000	–
185	0.5	1,166,933	Surface Pore
180	0.5	1,462,890	Surface Pore
175	0.5	>10,000,000	–
154	0.6	>10,000,000	–
148	0.6	>10,000,000	–
117	0.7	>10,000,000	–
116	0.7	>10,000,000	–
115	0.7	>10,000,000	–
113	0.7	>10,000,000	–

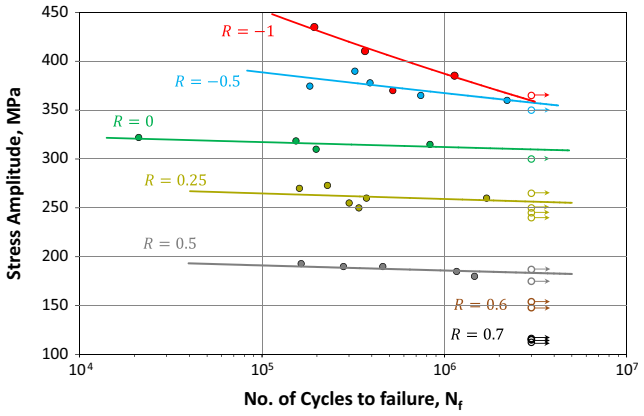

Fig. 3. *S–N* curve at different *R* ratios (arrow denotes the ran out specimens).

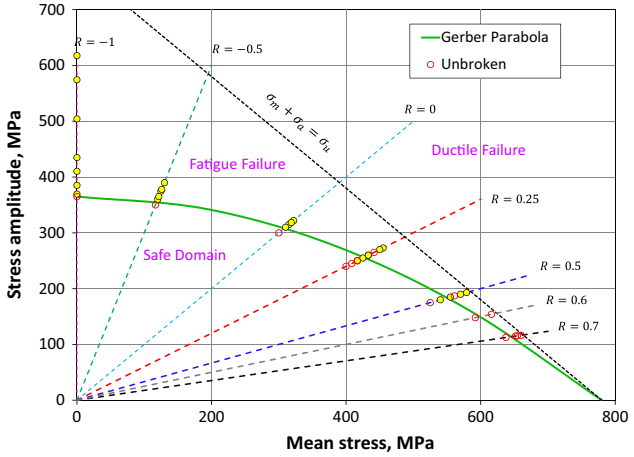

Fig. 4. Goodman plot of fatigue data with Gerber parabola.

along slip bands (Fig. 5(a)) and followed zig-zag paths with frequent deflections along grain or martensite laths boundaries (Fig. 5(b)). Asperity-induced closure must therefore be significant in such cases.

By contrast, at $R = 0.25$, 83% of the fatigue failures initiated from a defect, which, when internal gave rise to so called "fish eye" patterns (Fig. 6(a)). One-third of these defects were pores (Fig. 7) and two-third were debonded clusters of chemically inhomogeneous material (Fig. 8). SEM observations of mating fracture surfaces revealed a crater on one side and a cluster of non-homogeneous material on the other side (Fig. 8(a) and (b)). Chemical analysis using EDS showed much higher oxygen and carbon contents locally (Fig. 8(c)) than in the bulk. This inhomogeneous content thus had different mechanical properties than the matrix.

The fish eye looks brighter under the optical microscope, due to the absence of an oxide layer on the crack face because as long as the internal crack does not emerge at the free surface, it propagates without any contact with external air, "in vacuum". No ODA or FGA could be observed. SEM observations of the border of a fish-eye (Fig. 6(b)) reveal striking differences in the aspects of both sides. The inner part looks much smoother. It is also rather featureless, with nearly no traces of the underlying microstructure and without striations. But as soon as the crack propagates in air, well-marked crystallographic patterns evoking laths or grain boundaries, as well as fatigue striations can be observed (Fig. 6(c)).

Topographic analyses of the fracture surfaces around the defects using digital optical microscopy revealed the presence of tilted facets, inclined by 45° relative to the loading axis (Fig. 6 (d)), suggesting shear-driven crack initiation of Stage I type. As the crack grew, it became normal to the loading axis as if a stage I to stage II transition occurred. More or less radial twisted facets, covered with wear marks were however observed, within the fish-eye (Fig. 9), close to its external border.

5–10 μm deep, 20–100 μm wide sections normal to the fracture surface were cut in a specimen broken after 1.7 million cycles at $R = 0.25$ at various distances from the internal crack initiation site (Fig. 10). The sections cut 128 μm and 186 μm away from the initiation site (Fig. 10(c) and (d)) are located inside the fish-eye, while the section cut 600 μm away (Fig. 10(a) and (b)) is outside. While a rough crack profile ($R_p \approx 4$ μm) with many tiny secondary cracks can be observed outside the fish-eye, a much smoother crack profile appears inside the fish eye ($R_p \approx 0.6$ and 1 μm at 128 μm and 186 μm from the center, respectively) without secondary cracks. No modification of the mean grain size was observed below the fish eye surface.

For $R = 0.5$, 100% of the fatigue failure initiated from the surface, but contrary to what was observed at lower *R* ratios, a defect (machining mark or surface-braking pore) was always present at the initiation site, as illustrated in Table 3.

All the defects responsible for internal crack initiation were found near the surface (between 165 μm and 600 μm from the surface) and not randomly distributed on the fracture surface as expected for tensile fatigue tests, which are supposed to produce

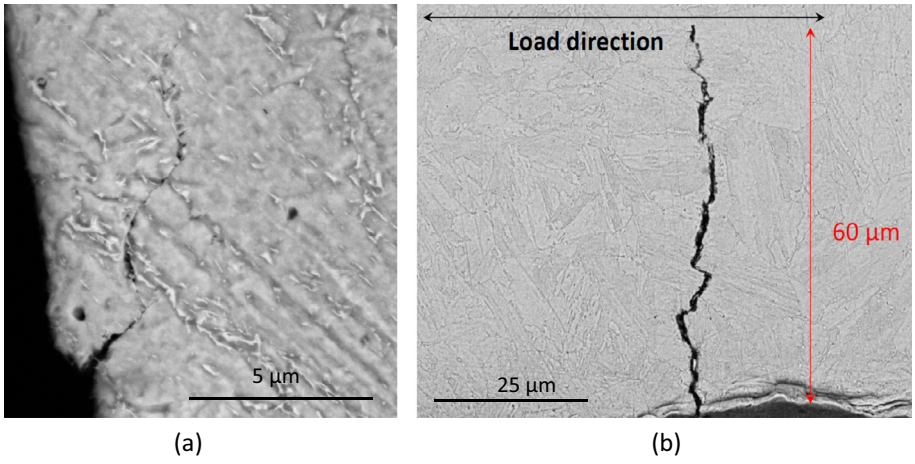

Fig. 5. (a) Surface crack initiation along a slip band for $R = -1$ and (b) zig-zag crack path with frequent deflections along laths or grain boundaries.

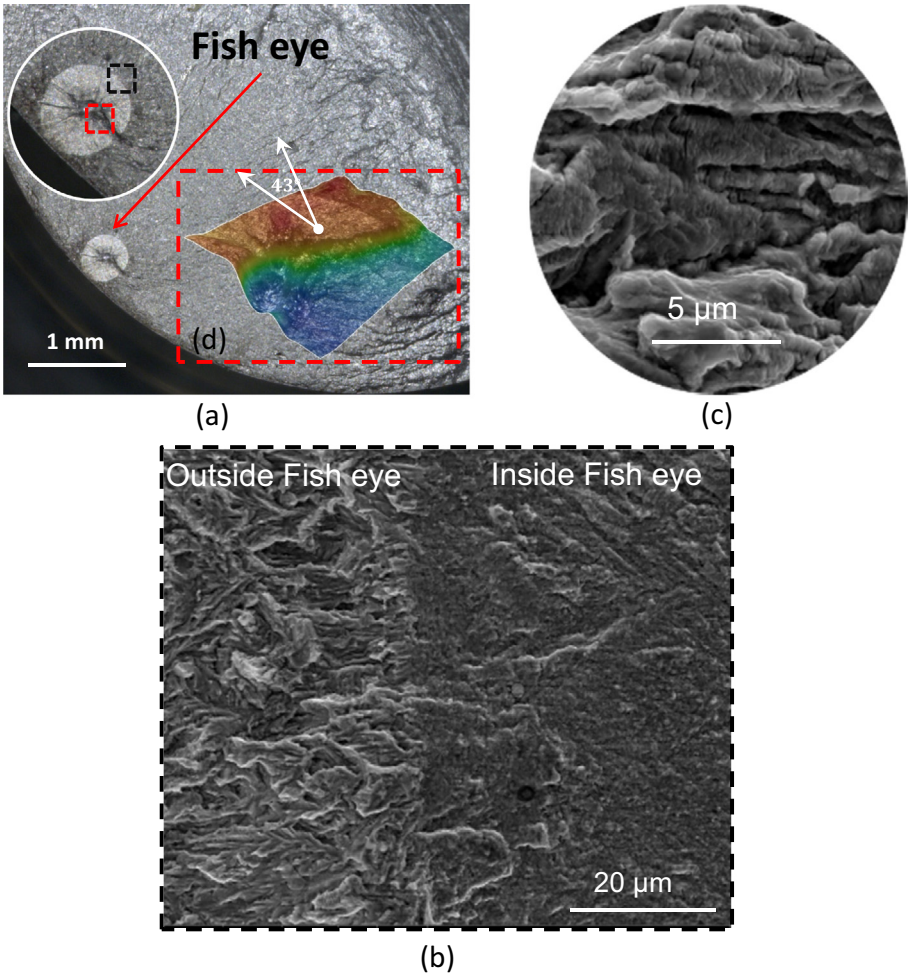

Fig. 6. (a) Fracture surface under optical microscope with "Fish eye", (b) SEM observation revealing the difference in aspects of roughness between crack growth in air and vacuum, (c) 3D topographic map around the pore, (d) striations outside the fish eye, 100 µm away from its border.

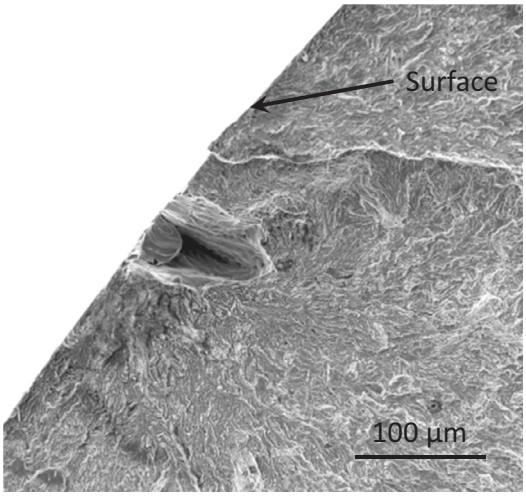

Fig. 7. Crack initiation from a surface Pore at $R = 0.5$.

a uniform stress field, provided any misalignment and bending stresses are avoided. The absence of such artifacts was verified. This suggests that machining-induced residual stresses, more or less redistributed by plastic flow during the first half cycle at high R ratio, were present in the specimens and played a role in the competition between surface and internal crack initiation.

2.3.2. The residual stress analyses

In order to clarify further, XRD analyses of surface residual stresses were done at three points on two virgin cylindrical specimens and revealed the presence of significant biaxial compressive residual stresses, scattered between −338 MPa and −407 MPa in the axial direction and between −208 and −345 MPa in the circumferential direction (Table 4). An in-depth profile of residual stresses is plotted in Fig. 11a. No correction of the calculated stresses, to take into account their redistribution due to material removal, was attempted. Therefore, this is not the exact distribution of residual stresses which should satisfy self-equilibrium conditions and thus exhibit an internal tensile peak. The profile of Full-width at half maximum (FWHM) (Fig. 11(b)) suggests that the depth affected by residual stresses is less than 60 µm, which is smaller than the depth of all internal crack initiating defects.

No macroscopic cyclic plasticity was observed during the high-cycle fatigue tests, but plastic flow often occurred during the first half cycle, especially at high R ratio, and some limited "ratcheting", was observed (utmost 3.5×10^{-3} strain was accumulated), depending on the stress range and mean stress. In fact, this limited apparent ratcheting, without any detectable cyclic plasticity, was suspected to correspond to a relaxation of those residual stresses. Thus, this potential relaxation was examined for each test.

Based on the superposition of the loading cycle with the maximum axial and circumferential residual stresses found in virgin specimens (−407 and −329 MPa, respectively), the minimum and

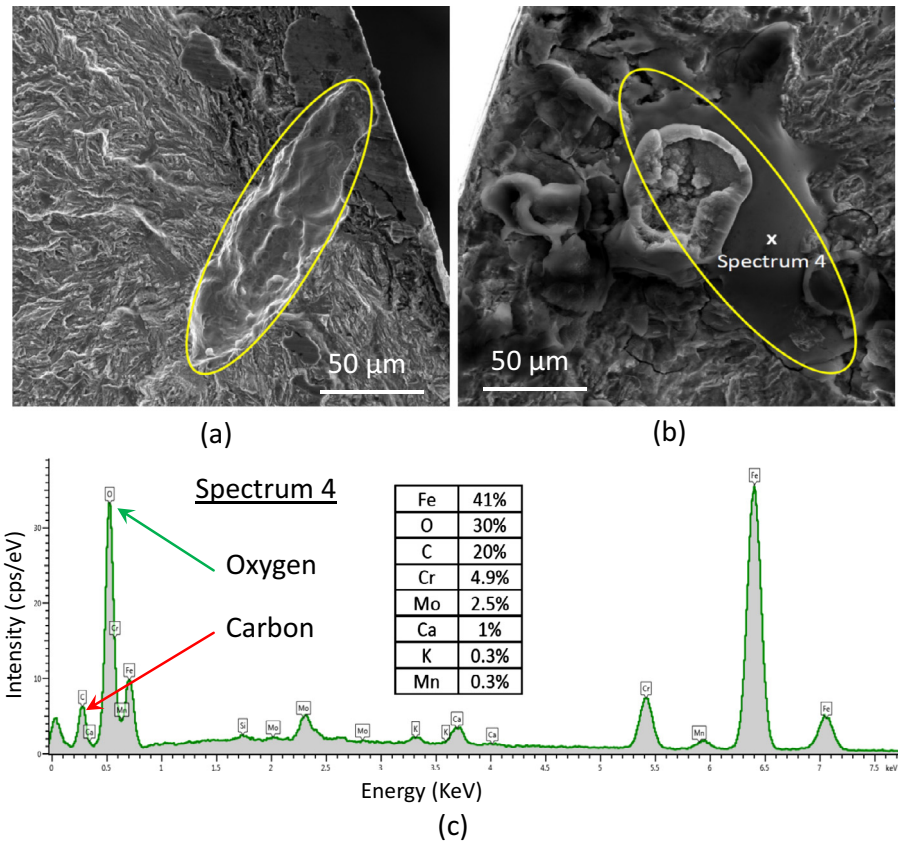

Fig. 8. (a) and (b) SEM images of the two halves of a specimen broken due to a crack initiated from a chemical inhomogeneity and (c) EDS spectrum of the inhomogeneous material.

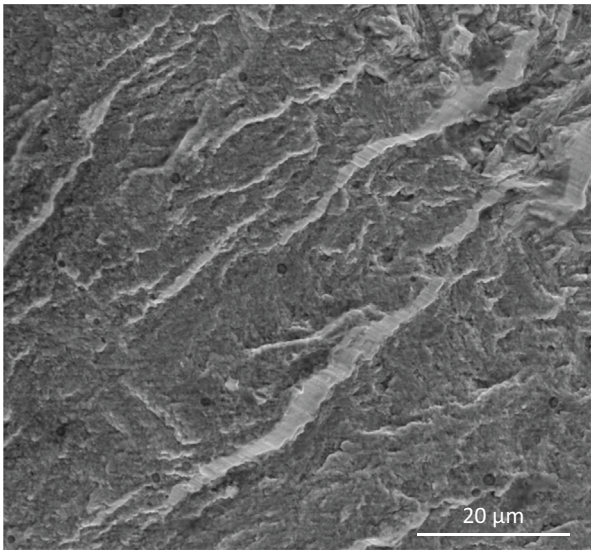

Fig. 9. Twisted facets near the external border of fish eye at $R = -0.5$ and $\Delta\sigma/2 = 360$ MPa.

maximum Von-Mises equivalent stresses (σ_{Mises}) over a cycle were computed and compared with the proportional limit ($\sigma_p = 600$ MPa): If either the min or max equivalent stress exceeded the proportional limit, the residual stresses were expected to relax. The previsions made with this simple criterion are compared with the residual stresses (σ_r) estimated after the fatigue tests for various R ratios and amplitudes (Table 5). In spite of a larger scatter in the measurements than on virgin materials, the following trends are found: for $R = -1$, the residual stresses are expected to relax, but compressive residual stresses exceeding 200 MPa were observed along the axial direction. For $R = -0.5, 0$ and 0.25, relaxation was neither expected nor observed. For $R = 0.5$, stress relaxation was expected only for the highest stress range but it seems to be partially relaxed only. For $R = 0.7$, relaxation was expected and indeed observed.

3. Discussion

3.1. Crack initiation

Surprisingly, the significant surface compressive residual stresses that partially or totally persisted after the tests did not inhibit surface crack initiation at $R = -1$, -0.5 or 0. In addition, when internal crack initiation occurred, the depth of the responsible defects were higher than that of the tensile peak of longitudinal residual stresses, which according to Fig. 11(b) is less than 60 µm. Thus, the transitions from a majority of cyclic plasticity-induced surface crack initiation for $R = -1$, -0.5 and 0 to a majority of internal crack initiation from a defect at $R = 0.25$ and then to defect-induced surface crack initiation for $R = 0.5$ do not seem to be controlled by residual stresses and their relaxation.

The potential role played by the changes in specimen's geometry in these transitions must be examined. For a uniform distribution of defects, the larger the gage volume, higher is the probability to find a large internal defect inside. In the 7 mm diameter specimens used for the tests at $R = 0.25$, the gage volume and thus this probability were smaller than in the 8 mm diameter specimens used for the tests at lower R ratio by a factor of 0.72. In spite of this,

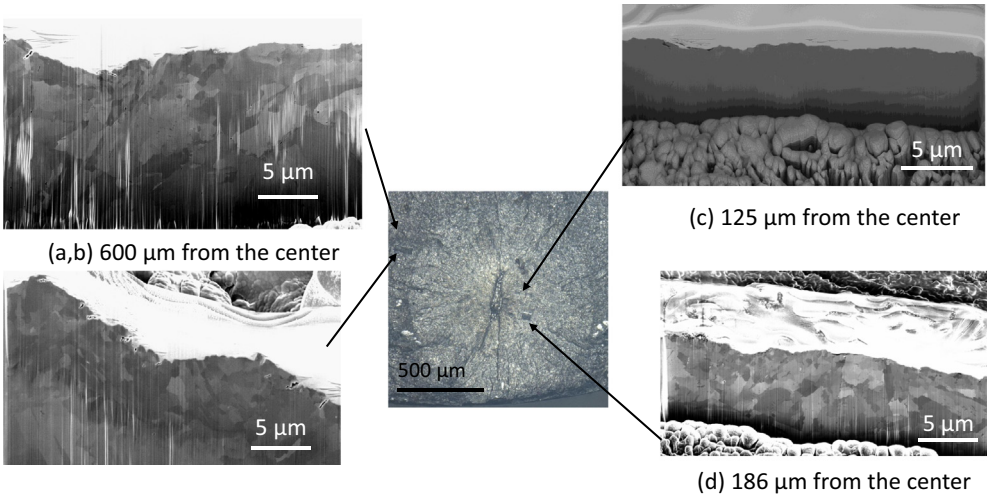

Fig. 10. SEM images of cross sections made with a FIB after platinum coating at various distances from a fish-eye center on the fracture surface of a specimen broken after 1,704,174 cycles at $R = 0.25$.

Table 4
Measured surface residual stresses on virgin specimens.

Specimen (position)	Residual stress (MPa)	
	Axial	Circumferential
1 (a)	−400 ± 8	−288 ± 9
1 (b)	−376 ± 10	−345 ± 12
1 (c)	−382 ± 9	−304 ± 9
2 (a)	−407 ± 5	−329 ± 11
2 (b)	−388 ± 8	−239 ± 14
2 (c)	−361 ± 12	−208 ± 14

the proportion of internal crack initiation (83%) was higher than in the previous cases. This effect, although it is based on a limited number of tests, thus suggests a mechanical effect of the higher R ratio and of the associated decrease in stress range.

For the tests ran at $R = 0.5$ and above, with diameter of 6 mm, the gage surface-to-volume ratio was increased by a factor of 1.17 compared to the specimens tested at $R = 0.25$. This should increase the probability for a large defect to be located on the surface rather than in the volume in the same proportion. Such a moderate effect cannot explain a change from 83% internal cracks at $R = 0.25$ to 100% defect-initiated surface cracks at $R = 0.5$.

Alternative explanations for this transition have been suggested below by a compared analysis of the stress and strain fields around an internal or surface-cutting inclusion and fracture mechanics arguments.

The analytical solution of Goodier [22] for the stress field around a spherical pore in an infinite elastic medium, yields a stress concentration factor K_t of 2.04 under uniaxial tension. For the stress amplitudes corresponding to the endurance limit at $R \geqslant 0$, this is sufficient to induce monotonic plastic flow ($2.04\sigma_{max} > \sigma_p$) around a pore, and in some cases, cyclic plastic flow and ratcheting ($2.04\Delta\sigma > 2\sigma_{yc}$, where σ_{yc} denotes the cyclic yield stress, substantially lower than σ_p in this steel, see Fig. A.2).

To analyze the stress and strain fields around an internal pore, a 3D finite element unit cell model containing 1/8th of a spherical pore was developed using quadratic hexahedron type elements (C3D20R) (Fig. 12). Symmetric boundary conditions were applied on the faces adjoining the pore. Elastic–plastic simulations were run for 100 cycles of the loadings leading to internal crack initiation. The constitutive equations with isotropic and non-linear kinematic hardening identified from several

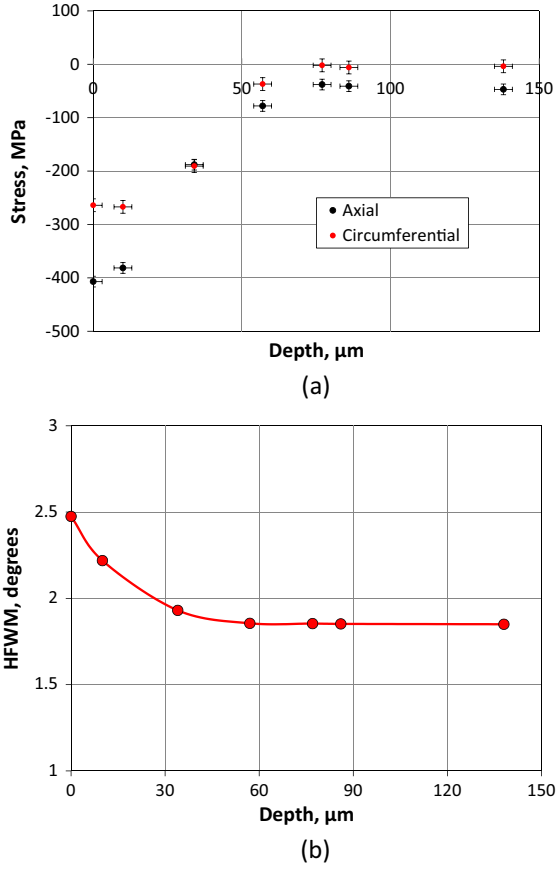

Fig. 11. (a) In-depth profile of initial surface residual stresses and (b) its corresponding profile of Full-width at Half maximum (FWHM) of the X-ray diffraction peaks measured in a virgin cylindrical specimen.

strain-controlled push–pull tests, as described in Appendix A, were used. For the example as illustrated in Fig. 13, at $\Delta\sigma = 520$ MPa and $R = 0.25$, the equivalent plastic strain at the edge of the pore reached 1.8% at the first peak load and ratcheting up to 2.5% strain was observed. After 100 cycles, the steady-state normal strain range was 0.5% and the local R ratio was close to −1, which is quite different from the far field stress ratio of 0.25.

Table 5
Surface residual stresses (σ_r) measured after fatigue tests far away from the fracture surface (>6 mm).

R	$\sigma_{applied}$ MPa		σ_{Mises} with σ_r, MPa		Relaxation expected	σ_r after fatigue, MPa	
	Min	Max	Min	Max		Axial	Tangential
−1	−385	385	318	690	Yes	−209 to −238	−211 to −244
−1	−365	365	311	675	Yes	−215 to −304	−180 to −185
−0.5	−240	480	370	560	No	−397 to −417	−247 to −281
−0.5	−243	487	375	563	No	−262 to −350	−256 to −285
0	0	637	374	486	No	−252 to −368	−244 to −248
0	0	620	374	473	No	−31 to −480	−197 to −229
0.25	170	680	294	522	No	−137 to −300	−236 to −251
0.5	386	772	319	601	Yes	45 to 74	−113 to −176
0.5	360	720	308	556	No	11 to −181	−118 to −312
0.7	539	770	411	600	Yes	−6 to −26	−12 to −32

Similar elastic–plastic F.E. computations were run for a surface-cutting pore. For that purpose, the same mesh was used, but a symmetry condition was removed, to represent the free surface. Due to a plane stress condition, the plastic strains reach higher values at the pore edges than for an internal pore under the same far field loading (Fig. 14). At the first peak load, the equivalent plastic strain at the edge of a surface pore is 2.0% as compared to 1.8% for an internal pore and after ratcheting during 100 cycles, it reaches 2.7% instead of 2.5%. However, the steady-state normal strain amplitude is same in both cases, i.e. 0.3%.

Even though the HCF tests were stress-controlled at a given R ratio, the F.E. computations clearly show that close to a pore, the local loading conditions are quite different and closer to strain-controlled low-cycle fatigue. That is why fatigue data collected in such conditions (Fig. A.1, in Appendix A) are considered to provide a reasonable baseline. Based on these fatigue data, the strain amplitude computed close to a pore should lead to crack initiation after a few thousand push–pull cycles only, in air. The lack of moist air and the sharp strain gradient on the one hand, and the higher stress triaxiality around an internal pore, on the other hand, certainly make fatigue crack initiation kinetics different from those in push–pull in air, but considering the above mentioned peak strain and amplitude, it seems quite improbable that crack initiation from internal pores controls the fatigue lives at $R = 0.25$.

Internal chemical heterogeneities produce smaller stress concentrations than internal pores of similar shape and size [22]. However, the data-points for failures initiated from the former or from the latter do not segregate on the Wöhler plot. This supports the idea that crack initiation constitutes a small fraction of the fatigue lives at $R = 0.25$. For the VHCF regime, there is a consensus about the predominance of the crack initiation stage from internal defects over the crack growth stage, such a conclusion does not seem to hold here.

Simulations were also run at $R = 0.5$ for $\Delta\sigma = 360$ MPa for a surface and internal pore respectively. At first peak load, an equivalent plastic strain of 3.9% (and 3.6% resp.) was found at the edge of the pore with ratcheting up to 4.1% (and 3.9% resp.) within 100 cycles. The normal strain amplitude at the 100th cycle was 0.2% in both cases, and the local R ratio −0.5 (and −0.4 resp.). These local conditions would probably be sufficient for early internal initiation from a pore at this R ratio as well.

Similar simulations ran for an internal pore at $R = 0.6$ and the highest stress amplitude (154 MPa) used in the experiments yielded an equivalent plastic strain of 4% on the edge of pore at first peak load but no ratcheting, due to the absence of cyclic plasticity. So, for $R \geqslant 0.6$, fatigue crack initiation seems improbable, in spite of the local stress concentration provided by a surface or internal pore (and even more, a surface or internal inhomogeneity). Anyway, should a crack initiate, it would probably be unable to grow, as discussed in the next section.

3.2. Crack growth

3.2.1. Crack growth mechanisms

The reduced roughness and the absence of striations on the fracture surfaces within the fish-eye are consistent with the literature on fatigue crack growth in vacuum [23,24]. McEvily and Gonzalez Velazquez [24] attribute the absence of striations in stainless steels fatigued in vacuum to the intense and diffused crack tip plasticity observed in this environment. The relatively large blunting of the tip resulting from such intense and diffused plastic flow would reduce the crack growth rate. By contrast, Hydrogen-Enhanced-Localized-Plasticity (HELP) [25–27] in moist air would induce coarse, localized crack tip plasticity, producing clear striations and leading to faster crack growth.

Note that all the defects responsible for internal crack initiation were found near the surface and that the border of each fish-eye was tangent to the free surface (as visible in Fig. 6(a)). The frontier of the fish-eye thus corresponds to a sudden ingress of the outside air into the crack.

The presence of intergranular facets on fatigue fracture surfaces formed at low crack growth rates in Ni–Cr–Mo–V and Cr–Mo steels has often been reported as a clear sign of combined temper and hydrogen embrittlement [23,28–31]. Islam et al. [28] have shown that a preliminary segregation of impurities during the heat treatment is necessary for this phenomenon, but that hydrogen released by a reaction of water vapor with the metal is also necessary and that the latter readily occurs in air at room-temperature and low crack growth rate.

In the present study, the absence of any intergranular or interlamellar facet or secondary crack within the fish-eye areas but their presence just outside the fish-eyes is consistent with this conclusion. It is also consistent with the lower roughness within the fish-eye than outside, since Liaw et al. [31] underlined that the presence of such facets increases with the roughness. The SEM observations of twisted and mated facets near the border of a fish eye (Fig. 9) and the FIB sections (Fig. 10) suggest a slight increase in roughness as the crack grows further from an internal defect with increasing ΔK. However, roughness-induced crack closure effects (RICC) are certainly less important during crack growth inside the fish-eyes than outside. In addition, oxide-induced crack closure as well as plasticity-induced crack closure (PICC) is absent inside fish-eye. The latter can be expected because of the low ΔK, plane strain/stress state for internal cracks and short crack lengths (although much larger than the former austenite grain size of 7 μm, so that LEFM can reasonably be used). To check that assumption, an axisymmetric FE model of penny shaped crack with a radius typical of that found for internal cracks was developed, with sufficient mesh refinement ahead of the crack tip (less than 1/10th of the reversed cyclic plastic zone size). Elastic–plastic simulations with periodic node release were run for similar cyclic loadings as

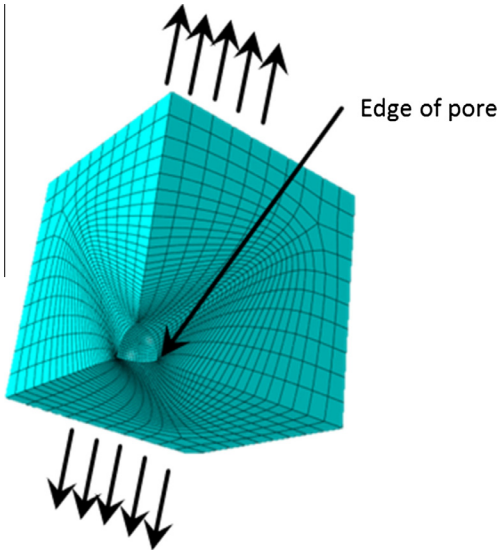

Fig. 12. A 3D Meshed unit cell model with quadratic hexahedron elements (C3D8R type) with symmetric boundary conditions on the faces adjoining the 1/8th pore.

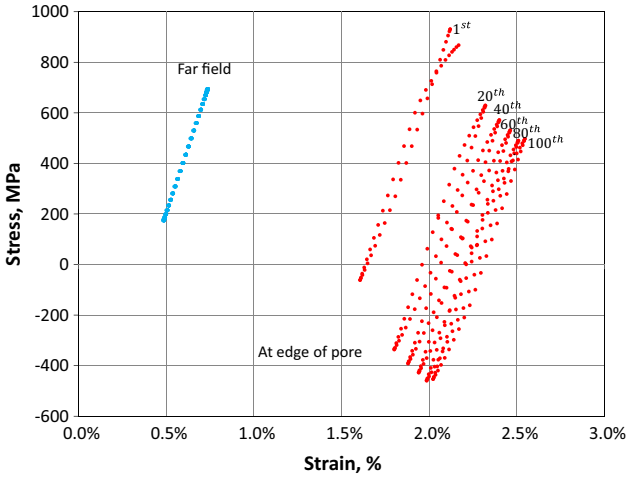

Fig. 13. Normal stress–strain loops at the edge of an internal spherical pore for $\Delta\sigma = 520$ MPa, $R = 0.25$.

those leading to internal cracking in the experiments. The closure level was evaluated at the second node behind the crack tip and no plasticity-induced closure was observed.

In summary, in the present study, internal cracks not only seem to grow with very few, if any, closure effects, but also without any assistance from moist air.

3.2.2. Crack growth threshold and kinetics

Suresh et al. [32] investigated fatigue crack growth kinetics and thresholds on a similar 2.25%Cr–1%Mo steel in air, dry helium and dry hydrogen for $R = 0.05$ and 0.75 (Fig. 15). They obtained $\Delta K_{threshold} = 7.1$ MPa $\sqrt{m}$ at $R = 0.05$ in air. In a reducing atmosphere (dry H_2), which nearly suppressed oxide-induced closure, the threshold at $R = 0.05$ dropped to 4.5 MPa $\sqrt{m}$, while in dry He it was 5 MPa $\sqrt{m}$. For $R = 0.75$ $\Delta K_{threshold}$ was 2.8 MPa $\sqrt{m}$ in air, as well as in dry hydrogen and 2.7 MPa $\sqrt{m}$ in dry helium. The latter value can probably be considered as a closure-free threshold.

In the present study, to analyze crack growth from internal defects, considered as elliptical, their major/minor semi-axes: 'a'

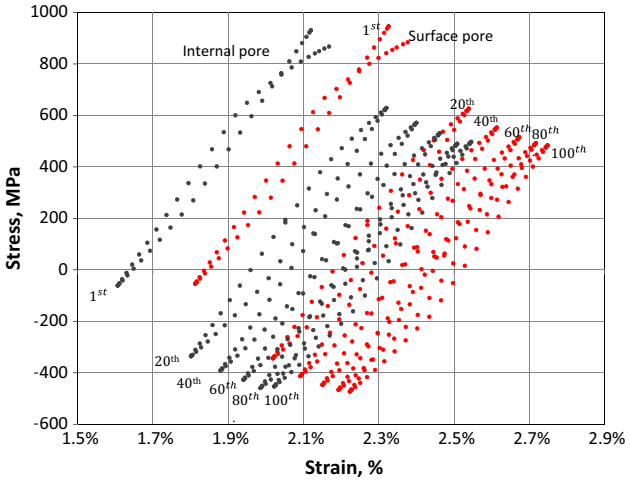

Fig. 14. Normal stress–strain loops at the edge of surface and internal spherical pores for $\Delta\sigma = 520$ MPa, $R = 0.25$.

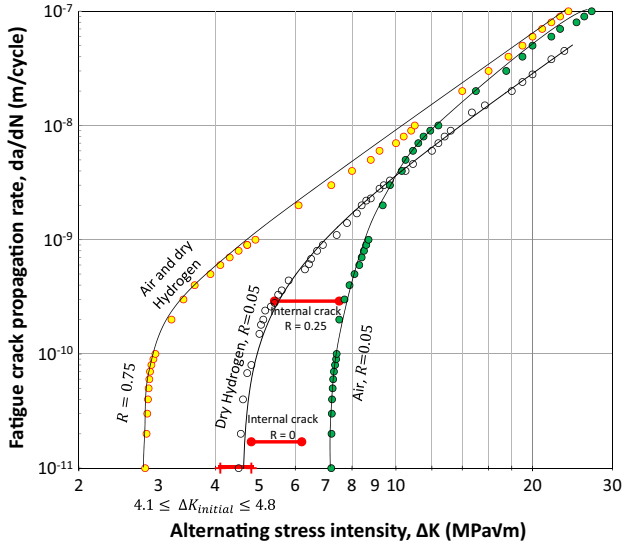

Fig. 15. Crack growth kinetics in 2.25Cr–1Mo steel at various R ratios in air and dry Hydrogen (Re-plotted from Suresh et al. [32]) with some data (red bars) from present study superimposed. (For interpretation of the references to color in this figure legend, the reader is referred to the web version of this article.)

and 'b', were measured and the stress intensity factor at any point along the crack front (designated by its angular position, ϕ, relative to the minor axis) was calculated for a remote stress range $\Delta\sigma$ as:

$$\Delta K_{I,max} = \frac{\Delta\sigma\sqrt{\pi b}}{E(k)} \tag{2a}$$

$$E(k) = \int_0^{\frac{\pi}{2}} \left(1 - k^2 \sin^2\phi\right)^{1/2} d\phi \tag{2b}$$

$$k^2 = 1 - \left(\frac{b}{a}\right)^2 \tag{2c}$$

ΔK_I was calculated by taking into account only the tensile part of the cycle. The maximum ΔK for an elliptical crack occurs at the end point of the minor axis ($\phi = 0$). Both the initial and final maximum ΔK_I (considering the defect as a crack in the former case and at the border of the fish eye in the latter) were computed. The ΔK_I

values computed with the approximate expression from Murakami [16] (Eq. (3)) were less than 8% different from those computed with Eq. (2a).

$$\Delta K_I = \beta \sigma_{max} \sqrt{\pi \sqrt{area}} \tag{3}$$

where "area" denotes the area of the defect projected on the plane normal to the tensile stress, $\beta = 0.5$ for an internal defect and $\beta = 0.65$ for a surface defect.

For all the observed internal cracks, the initial ΔK_I lies between 4.1 and 4.8 MPa $\sqrt{m}$ (see the bar superimposed on Fig. 15 and the comparison with threshold data in air from Suresh et al. [32] and Liaw et al. [31] in Fig. 16). In particular, the values found for the two specimens broken at $R = -0.5$ are close to the specimens broken at $R = 0.25$. This is consistent with the idea of Stewart [23] and Vasudevan et al. [33], that the threshold ΔK for crack growth in vacuum is much less dependent on the R ratio than in air, although both studies, contrary to the present one, considered only positive R ratios.

Anyway, based on the threshold of 7.1 MPa $\sqrt{m}$ that Suresh et al. [32] obtained in air at $R = 0.05$, and the usually accepted idea that vacuum makes crack growth slower and the threshold higher, the internal cracks found here at $R = -0.5$ should not propagate. The fact that these cracks actually grew at such a low ΔK in spite of a lower R ratio suggests either that the reduction in crack closure compensates (or even overcompensates) the lack of environmental assistance to crack growth or that some moist air trapped in the pore assists incipient crack growth. However, no ODA or crystallographic, intergranular or inter-lamellar area, expected in case of environment-assisted crack growth was observed around the defects, but directly a smooth featureless surface, so that the first explanation is preferred.

A specimen first survived 3 million cycles at $\sigma_a = 300$ MPa at $R = 0$ and was then reloaded at $\sigma_a = 260$ MPa at $R = 0.25$ until it failed after 373,900 cycles. A beach mark was found within the fish eye indicating the position of the crack front by the end of the first loading block, and thus allowing the computation of the mean crack growth rates during the first block (1.7×10^{-11} m/cycle, while ΔK was increasing from 4.8 to 6.2 MPa $\sqrt{m}$) and the second block (2.9×10^{-10} m/cycle, while ΔK was increasing from 5.4 to 7.5 MPa $\sqrt{m}$). For the former estimate, the crack initiation stage was neglected. These data are superimposed on the kinetics curves re-plotted from Suresh et al. [32] (Fig. 15). These data, corresponding to internal crack growth at $R = 0$ and $R = 0.25$, clearly fall on the left side of the kinetics curve obtained in air at $R = 0.05$.

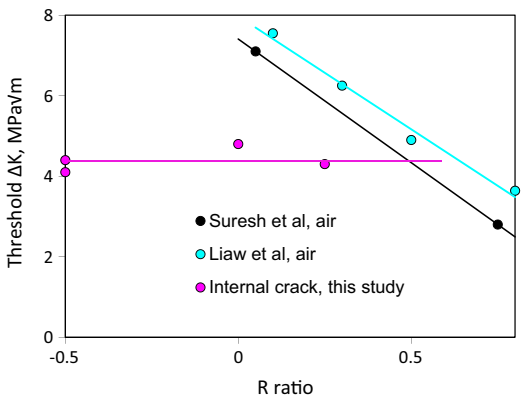

Fig. 16. Comparison of threshold ΔK values issued from Liaw et al. [31], Suresh et al. [32] and the present study.

For $R = 0.5$, ΔK was found to be 3.7–3.9 MPa $\sqrt{m}$ for surface defects as shown in Fig. 7. No threshold data is available for crack growth in air at that R ratio in the paper by Suresh et al. [32], but according to the extensive $\Delta K_{threshold}$ versus R database gathered by Bulloch [34] for steels with a tempered martensite microstructure, these values are still compatible with crack growth and thus fatigue failure, as observed. Comparatively, according to Eq. (3), ΔK_I for a crack initiated from an internal defect of similar size would be between 2.85 and 3 MPa $\sqrt{m}$, which is clearly below the scatter-band of threshold ΔK values reported by Bulloch for this R ratio, in air [34], and also well below the smallest ΔK computed for any of the internal cracks observed (see Fig. 16). This explains why at $R = 0.5$, only cracks initiated from surface defects were observed.

By contrast, the ΔK computed for the cyclic loading conditions used at $R = 0.6$ or 0.7, assuming the presence of the most critical observed defect in a specimen (which is 199 μm by 66 μm wide), comes out to be around 2 MPa $\sqrt{m}$. Comparing it with the 2.8 MPa $\sqrt{m}$ threshold measured, in the absence of closure by Suresh et al. [32] at $R = 0.75$ in air, dry H_2 or He, it seems that such defects would not propagate. This explains why specimens at very high R ratio did not fail by fatigue within 10^7 cycles.

3.3. Concluding remarks

A decrease in the slope of Wöhler curves and an increased scatter in fatigue lives were observed when the R ratio rose. Similar effects have been reported in literature (see for example Fig. 6.29 in [16]). It can be suggested that for $R < 0$ and thus relatively high stress ranges, that allow the threshold ΔK for crack growth to be surpassed easily for very small cracks, the crack growth rates and thus the fatigue lives vary significantly with the loading range. By contrast, for higher R ratios and thus smaller stress ranges, the fatigue lives become more and more dependent on the presence of defects large enough to allow the threshold ΔK to be reached. The scatter in fatigue lives increases and the slope of Wöhler curves decreases, which makes the safe fatigue design of structures tricky. It might be reasonable to consider R-ratio dependent safety factors but Murakami [16] advised not to use such (more or less arbitrary) safety factors in design, rather a lower bound for the endurance limit issued from a statistical analysis of defects size distribution. Although, such an approach is more rational and based on fracture mechanics, it is however not clear if it would capture the R-ratio dependence of the scatter in fatigue lives.

Since in the present study, the crack initiation sites are controlling the variation of endurance limit with the R-ratio, Eq. (1a) can be used only in the narrow range R = 0.25–0.5. Based on Vickers Hardness ($H_V = 267$) and the largest possible defect, these equations predict endurance limits of 213 and 195 MPa, respectively, for $R = 0.25$ (while the measured value is 255 MPa), and 195 and 179 MPa, for $R = 0.5$ (while the measured value is 187 MPa). The agreement is good for the latter R ratio, but not for the former, and these equations underestimate the R ratio dependency of the endurance limit.

Finally, a tentative map of the mechanisms that control the endurance limit at 3 million cycles depending on the mean stress or R ratio is shown in Fig. 17. For low mean stresses, surface crack initiation merely due to cyclic plasticity predominates, but when the mean stress rises and the amplitude decreases, the stress concentration provided by a defect becomes necessary for crack initiation. At intermediate R ratios and amplitudes, cracks are able to grow from surface or internal defects, but as the R ratio is further increased (to 0.5 in the present case) and the amplitude decreased, only the cracks grown in air from surface defects which, according

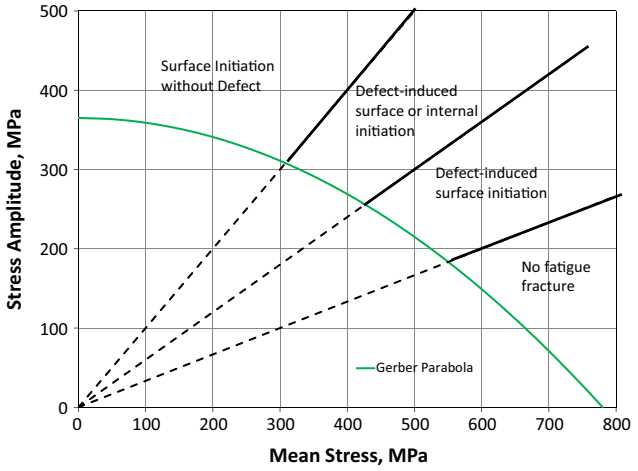

Fig. 17. A tentative map of the mechanisms of fatigue failure depending upon the mean stress or R-ratio at 3 million cycles.

to Eq. (3), undergo a higher ΔK than those from internal defects of similar size can cause failure. For even higher R ratios, the amplitude becomes too small to allow any crack to grow, be it in air or in vacuum. Note that this map would change if a larger number of cycles was chosen to define the endurance limit: the defect-controlled fracture domain would probably extend to lower mean stresses/R ratios. The map, which is plotted for uniaxial loading, would also change for biaxial loading, because the stress concentration around a defect depends on the far-field stress state [22]. For example, the K_t around an internal spherical pore is 1.36 under equibiaxial tension instead of 2.04 in uniaxial tension. The defect-controlled fracture domain is then expected to shrink. High-cycle fatigue tests in biaxial tension-induced by combined tension and internal pressure on tubular specimens are in progress and might shed light on this question.

4. Conclusions

Stress-controlled fatigue tests were run at different R ratios up to at most 3 million cycles on a 2.5%Cr–1%Mo steel. The fatigue lives, as well as the slope of the S–N curves decreased with increasing R. The endurance limit followed Gerber's parabola, although no fatigue fracture was observed above $R = 0.6$ at least up to 10^7 cycles.

Surface crack initiation without any defect involved was most often observed for $R = -1,\ -0.5$ and 0, while an R ratio of 0.25 triggered crack initiation from either surface or internal pores or chemically inhomogeneous areas leading, in the latter case, to "fish-eye" patterns for relatively low numbers of cycles. A further increase in R ratio to 0.5 promoted only defect-initiated surface cracks.

In spite of significant level of machining residual stresses within a thin surface layer, their R-ratio and amplitude dependent relaxation did not seem to control the crack initiation sites.

3D elastic–plastic F.E. computations of the stress/strain fields around internal and surface pores, as well as fracture mechanics arguments were used to rationalize the observed transitions in crack initiation mode related to changes in R ratio. Internal cracks seemed to grow with very few, if any, closure effects. In the material investigated, this might compensate the absence of assistance from moist air, and explain their propagation at a ΔK which is substantially lower than the threshold measured in air and which is apparently the same for $R = -0.5,\ R = 0$ and $R = 0.25$.

Acknowledgment

The authors acknowledge the assistance of Dr. E. Heripre for FIB sectioning and observations with a dual beam microscope bought within the Equipex Matmeca funding program.

Appendix A. Identification of elastic–plastic constitutive equations and low-cycle fatigue behavior for F22 steel

Fully-reversed strain-controlled push–pull tests were run until failure at a strain rate of $2 \times 10^{-3}\ s^{-1}$ for total strain amplitudes of $\pm 0.215\%$, $\pm 0.3\%$, $\pm 0.75\%$, and $\pm 1.2\%$ using an extensometer with 10 mm gage length. The number of cycles to failure is plotted versus the strain amplitude on Fig. A.1. The present material exhibits some cyclic softening, as illustrated by Fig. A.2. The recorded evolutions of the stress and strain were used to identify constitutive equations using Von Mises yield function and two non-linear kinematic hardening variables denoted by X_1 and X_2 and one isotropic hardening variable denoted by R, according to the following equations:

Yield function:

$$J_2(\sigma - X) - R = 0 \tag{A.1}$$

$$J_2(\sigma - X) = \sqrt{\frac{3}{2}(\sigma - X)^D : (\sigma - X)^D} \tag{A.2}$$

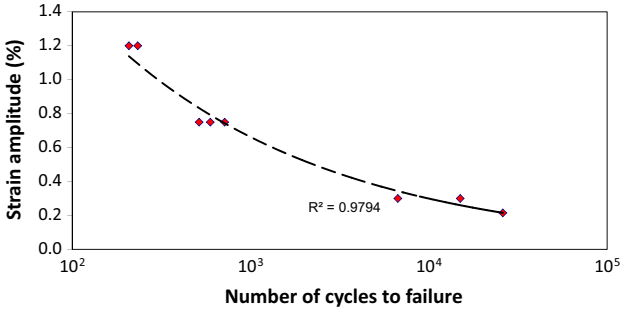

Fig. A.1. Fatigue lives of F22 steel for strain-controlled fully-reversed push–pull tests.

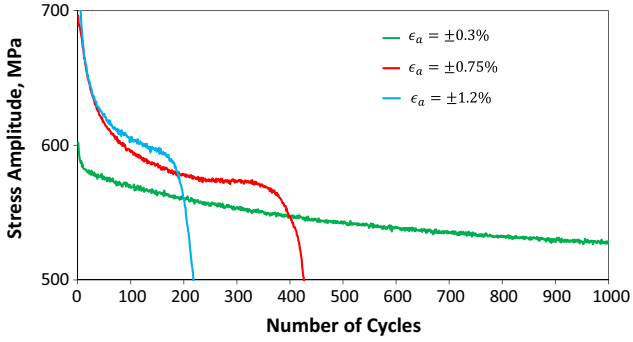

Fig. A.2. Evolution of stress amplitude during the early stage of strain-controlled push–pull tests.

Table A.1
Coefficients identified for the elastic–plastic constitutive equations.

R_0 (MPa)	Q (MPa)	b	C_1 (GPa)	γ_1	C_2 (GPa)	γ_2
343	−130	2	351	1140	12.5	32

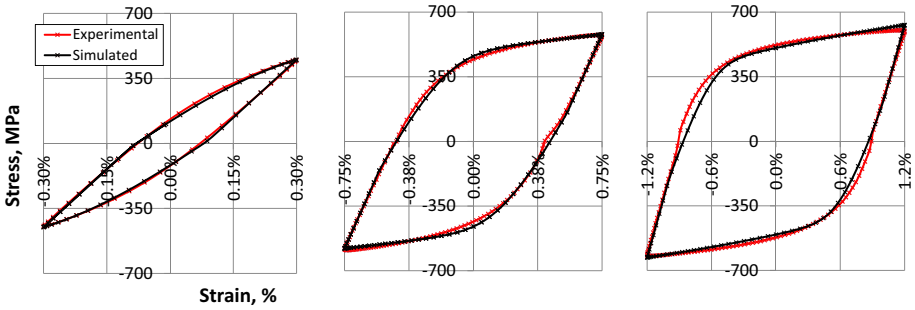

(a) $\epsilon_a = \pm 0.3\%$ (b) $\epsilon_a = \pm 0.75\%$ (c) $\epsilon_a = \pm 1.2\%$

Fig. A.3. Stress strain loops at half-life during strain-controlled push–pull tests and simulated loops using the constitutive equations.

where J_2 denotes the second invariant of stress tensor.

Isotropic hardening:

$$R = R_0 + Q(1 - e^{-b\epsilon_p}) \tag{A.3}$$

Kinematic hardening:

$$\delta X_i = C_i \delta\epsilon_p - \gamma X_i \delta p \quad i = 1, 2 \tag{A.4}$$

where δp denotes the cumulated plastic strain:

$$\delta\dot{p} = \sqrt{\frac{2}{3}\dot{\epsilon_p} : \dot{\epsilon_p}} \tag{A.5}$$

where R_0, Q, b, C_i and γ_i are material parameters. The optimization module of the Zset F.E. code [35] was used to identify the seven parameters reported in Table A.1, based on repeated simulations of the push–pull tests with varying values of the parameters, so as to minimize, via Runge and Kutta's algorithm, an error function which characterizes the sum other all data-points of the quadratic distance between measured and computed stresses. Fig. A.3 compares the measured and simulated stress–strain loops at mid-life.

References

[1] Murakami Y, Nomoto T, Ueda T. On the mechanism of fatigue failure in the super long life regime ($N > 10^7$) cycles. Part 1: Influence of hydrogen trapped by inclusions. Fatigue Fract Eng Mater Struct 2000;23:893–902.

[2] Ochi Y, Matsamura T, Masaki K, Yoshida S. High-cycle rotating bending fatigue property in very long-life regime of high strength steels. Fatigue Fract Eng Mater Struct 2002;25:823–30.

[3] Furuya Y. Specimen size effects on gigacycle fatigue properties of high-strength steel under ultrasonic fatigue testing. Scripta Mater 2008;58:1014–7.

[4] Furuya Y. Visualization of internal small fatigue crack growth. Mater Lett 2013;112:139–41.

[5] Ogawa T, Stanzl-Tschegg S, Schönbauer B. A fracture mechanics approach to interior fatigue crack growth in the very high cycle regime. Eng Fract Mech 2014;115:241–54.

[6] Mughrabi H. On multi-stage fatigue life diagrams and the relevant life-controlling mechanisms in ultrahigh-cycle fatigue. Fatigue Fract Eng Mater Struct 2002;25:755–64.

[7] Shiozawa K, Morii Y, Nishino S, Lu L. Subsurface crack initiation and propagation mechanism in high-strength steel in a very high cycle fatigue regime. Int J Fatigue 2006;28(11):1521–32.

[8] Naito T, Ueda H, Kikuchi M. Fatigue behavior of carburized steel with internal oxides and nonmartensitic microstructure near the surface. Metall Trans A 1984;15(7):1431–6.

[9] Murakami Y, Nomoto T, Ueda T. On the mechanism of fatigue failure in the super long life regime ($N > 10^7$) cycles. Part II: A fractographic investigation. Fatigue Fract Eng Mater Struct 2000;23(11):903–10.

[10] Nakamura T, Oguma H, Shinohara Y. The effect of vacuum-like environment inside sub-surface fatigue crack on the formation of ODA fracture surface in high strength steel. Proc Eng 2010;2:2121–9.

[11] Petit J, Sarrazin-Baudoux C. An overview on the influence of the atmosphere environment on ultra-high-cycle fatigue and ultra-slow fatigue crack propagation. Int J Fatigue 2006;28:1471–8.

[12] Sakai T, Harada H, Oguma N. Crack initiation mechanism of bearing steel in high cycle fatigue. Fract Nano Eng Mater Struct 2006:1129–30.

[13] Zhu M, Xuan F. Effect of microstructure on appearance of near-threshold fatigue fracture in Cr–Mo–V steel. Int J Fract 2009;159:111–20.

[14] Li W, Sakai T, Wakita M, Mimura S. Effect of surface finishing and loading condition on competing failure mode of clean spring steel in very high cycle fatigue regime. Mater Sci Eng 2012;552:301–9.

[15] Li W, Yuan H, Sun Z, Zhang Z. Surface vs. interior failure behaviors in a structural steel under gigacycle fatigue: failure analysis and life prediction. Int J Fatigue 2014;64:42–53.

[16] Murakami Y. Metal fatigue: effects of small defects and nonmetallic inclusions. Elsevier Science; 2002.

[17] Kovacs S, Beck T, Singheiser L. Influence of mean stresses on fatigue life and damage of a turbine blade steel in the VHCF-regime. Int J Fatigue 2013;49:90–9.

[18] Persent E, Guesnon J, Leroy J, Richard F, Laval E. Development of a 14-inch ID high-pressurehybrid riser for SBOP drilling. Oil Gas Sci Technol – Rev IFP 2010;65:315–30.

[19] Achouri M, Gildemyn E, Germain G, Dal Santo P, Potiron A. Influence of the edge rounding process on the behaviour of blanked parts: numerical predictions with experimental correlation. Int J Adv Manuf Technol 2014;71:1019–32.

[20] Noyan I, Cohen JB. Residual stress – measurement by diffraction and interpretation; 1987.

[21] Gerber W. Calculation of allowable stresses in iron structures. Z Bayer Archit Ing Ver 1874;6(6):101–10.

[22] Goodier J. Concentration of stress around spherical and cylindrical inclusions and flaws. Trans ASME 1933;55(7):39.

[23] Stewart A. The influence of environment and stress ratio on fatigue crack growth at near threshold stress intensities in low-alloy steels. Eng Fract Mech 1980;13:463–78.

[24] McEvily A, Gonzalez Velazquez J. Fatigue crack tip deformation processes as influenced by the environment. Metall Trans A 1992;23:2211–21.

[25] Beachem C. A new model for hydrogen assisted cracking (hydrogen embrittlement). Metall Trans A 1972;3:437–51.

[26] Birnbaum H, Sofronis P. Hydrogen-enhanced localized plasticity-a mechanism for hydrogen-related fracture. Mater Sci Eng: A 1994;176:191–202.

[27] Lynch S. 2 – Hydrogen embrittlement (HE) phenomena and mechanisms. In: Raja V, Shoji T, editors. Stress corrosion cracking, woodhead publishing series in metals and surface engineering. Woodhead Publishing; 2011. p. 90–130.

[28] Islam M, Bowen P, Knott J. Intergranular fracture on fatigue fracture surface of 2.25Cr–1Mo steel at room temperature. J Mater Eng Perform 2005;14(1):28–36.

[29] Ritchie R. Influence of impurity segregation on temper embrittlement and on slow fatigue crack growth and threshold in 300-M high strength steel. Metall Trans A 1977;8:1131–9.

[30] Hénaff G, Petit J, Bouchet B. Environmental influence on the near-threshold fatigue crack propagation behaviour of a high strength steel. Int J Fatigue 1992;14(4):211–8.

[31] Liaw P, Saxena A, Swaminathan V, Shih T. Effect of load ratio and temperature on the near-threshold fatigue crack propagation behaviour in a CrMoV steel. Metall Mater Trans A 1983;14:1631–40.

[32] Suresh S, Zamiski G, Ritchie R. Oxide-induced crack closure: an explanation for near-threshold corrosion fatigue crack growth behavior. Metall Trans A 1981;12(8):1435–43.

[33] Vasudevan A, Sadananda K, Holtz R. Analysis of vacuum fatigue crack growth results and its implications. Int J Fatigue 2005;27:1519–29.

[34] Bulloch J. The influence of mean stress or R ratio on the fatigue crack threshold characteristics of steels – a review. Int J Press Vess Pip 1991;47(3):263–92.

[35] http://www.zset-software.com/products/zebulon/.